

Article

Development of a Raman Temperature LiDAR with Low Energy and Small Aperture by Parameter Optimization

Bingqing Xu ¹, Honglong Yang ², Jinhong Xian ^{2,3,*} , Wenjing Xu ¹, Yuli Han ¹ , Chong Chen ¹, Yu Gong ⁴, Dongsong Sun ¹ and Xuan Wang ^{5,*} 

¹ School of Earth and Space Sciences, University of Science and Technology of China, Hefei 230026, China; bingqing@mail.ustc.edu.cn (B.X.); xxwwjj@mail.ustc.edu.cn (W.X.); hanyuli@ustc.edu.cn (Y.H.); cchan@mail.ustc.edu.cn (C.C.); sds@ustc.edu.cn (D.S.)

² Shenzhen National Climate Observatory, Meteorological Bureau of Shenzhen Municipality, Shenzhen 518040, China; yanghonglong@weather.sz.gov.cn

³ School of Atmospheric Sciences, Nanjing University, Nanjing 210023, China

⁴ Guangdong Ecological Meteorological Center, Guangzhou 510640, China; gongy@gd121.cn

⁵ School of Remote Sensing and Information Engineering, Wuhan University, Wuhan 430072, China

* Correspondence: jhxian@mail.ustc.edu.cn (J.X.); xuan.wang@whu.edu.cn (X.W.)

Abstract: The range of detection and accuracy of currently available Raman temperature LiDAR systems are primarily improved by increasing the energy or the aperture of the receiving telescope. However, this does not lead to a corresponding linear increase in the distance of detection and accuracy of the system. In this paper, the authors construct a simulation model and optimize its parameters to develop a Raman temperature LiDAR with low energy and a small aperture that has a maximum distance of detection of over 5 km during the day and over 10 km at night. The profile of the atmospheric temperature obtained through field tests was in good agreement with the results of a radiosonde. The maximum correlation between the Raman temperature LiDAR and the radiosonde was 0.94 at night and 0.81 during the day. The results showed that the proposed Raman temperature LiDAR, with low energy and a small aperture, can provide reliable data on the temperature in the troposphere throughout the day.

Keywords: Raman temperature LiDAR; low energy; small aperture; pure rotational Raman; parameter optimization



Citation: Xu, B.; Yang, H.; Xian, J.; Xu, W.; Han, Y.; Chen, C.; Gong, Y.; Sun, D.; Wang, X. Development of a Raman Temperature LiDAR with Low Energy and Small Aperture by Parameter Optimization. *Photonics* **2023**, *10*, 716. <https://doi.org/10.3390/photonics10070716>

Received: 24 May 2023

Revised: 15 June 2023

Accepted: 21 June 2023

Published: 22 June 2023



Copyright: © 2023 by the authors. Licensee MDPI, Basel, Switzerland. This article is an open access article distributed under the terms and conditions of the Creative Commons Attribution (CC BY) license (<https://creativecommons.org/licenses/by/4.0/>).

1. Introduction

Temperature is one of the most important state variables of the earth's atmosphere and plays an important role in climatology, meteorology, atmospheric dynamics, and chemistry [1]. The atmosphere can be divided into the troposphere, stratosphere, mesosphere, and thermosphere according to temperature and density. This paper focuses on tropospheric temperature detection. A long-term continuous observation of tropospheric temperature profiles is extremely crucial for numerical weather prediction, the investigation of many atmospheric processes, and climate monitoring [2]. The temperature gradient together with humidity also governs atmospheric stability. In addition, atmospheric temperature also has an impact on human life. For instance, air quality in middle and high latitudes declines significantly in winter due to radiative cooling at night and strong inversion near the ground [3]. LiDAR has been used with various technologies to detect atmospheric temperature profiles over the past decade [4], namely the rotational Raman technique, the integration technique, and the resonance fluorescence technique, as well as the high-spectral-resolution LiDAR technique and differential absorption LiDAR. For all-day measurements in the troposphere, rotational Raman LiDAR has proven to be the most reliable technology at present [5,6].

Raman LiDAR for temperature detection has been developed steadily in recent years, and both the instrument and the data analysis methods have gradually improved to achieve a better detection performance [7]. The use of the temperature dependence of the pure rotational Raman (PRR) spectra for tropospheric temperature profiling was introduced by Cooney [8]. The range of the detection and accuracy of currently available Raman temperature LiDAR systems can be primarily improved by increasing the energy or the aperture of the receiving telescope. In 1976, Cooney and Pina developed a Raman temperature system by using a laser with a pulse energy of 40 mJ and a receiving telescope with an aperture of 400 mm to measure the temperature distribution at a range of altitude of 600 to 1100 m, with a statistical error of up to 4 K at 1100 m [9]. In 2000, Behrendt and Reichardt established a Raman temperature system with a laser with a pulse energy of 200 mJ, and a large receiving telescope with a diameter of 900 mm [10]. Its statistical error in measuring the atmospheric temperature was smaller than 1 K and its detection distance was as far as 18 km. In 2004, Di Girolamo et al. established a Raman temperature system by using a 355 nm Nd:YAG laser with a pulse energy of 350 mJ and a receiving telescope with an aperture of 760 mm. The system extended nighttime measurements with an error in the temperature of smaller than 1.5 K over a distance of 15 km, a vertical resolution of 600 m, and an integration time of 90 min [11]. In 2015, Hama et al. from Hohenheim University developed a Raman LiDAR system to measure the temperature, humidity, and optical parameters of the aerosol throughout the day. The statistical error in its measurements of the daytime temperature below an altitude of 1020 m was smaller than 1 K [6]. The laser used in the system had an energy of 200 mJ, and the receiving telescope had an aperture of 400 mm. In 2018, Weng et al. of Wuhan University established a temperature LiDAR system with a detection distance of 6.5 km [12]. The system used a laser with an energy of up to 800 mJ and a receiving telescope with an aperture of 200 mm. It is evident from the above that increasing the energy and aperture of the system does not lead to a linear increase in its detection distance and accuracy. Selecting the optimal parameters for a Raman temperature system with known requirements in terms of detection is a problem that requires further research.

In this paper, we investigate the means of developing a low-energy, small-aperture Raman temperature LiDAR that can meet the requirements of the accuracy and distance of detection. We examine the impact of various parameters (wavelength and pulse energy of the laser emitter, and the optical parameters of the interference filters) on its performance in terms of detection by simulating echo signals under different conditions of the aerosol, with the aim of determining the optimal system parameters. Section 2 introduces the principle of the simulations while details of the numerical analysis are provided in Section 3. Finally, Sections 4 and 5 present examples of measurements and a summary of the results.

2. Methodology

A laser with wavelength λ_0 interacts with the atmosphere and passes through the LiDAR receiving system. The number of Raman echo photons detected by the photon detector is [13]:

$$N_{RR}(z, T) = ft \frac{E_0 \lambda_0}{hc} \eta \frac{A_R O(z)}{z^2} \Delta z N(z) \left[\sum_{i=O_2, N_2} \sum_{J_i} f(\lambda_{J_i}) \varepsilon_i \left(\frac{d\sigma}{d\Omega} \right)_{\pi}^{RR,i} (J_i, T) \right] T_{atm}, \quad (1)$$

where f is the repetition rate of the laser, t is the integration time, E_0 is the laser pulse energy, h is the Planck constant ($m^2 \text{ kg/s}$), c is the speed of light (ms^{-1}), η is the system efficiency at wavelength λ_0 , A_R is the surface area of the receiving telescope, $O(z)$ is the overlap function of the laser beam and the receiver field of view, Δz is the range resolution, $N(z)$ is the spatial density of air molecules, J is the rotational quantum number, $f(\lambda_{J_i})$ is the transmission of the receiver at wavelength λ_{J_i} , ε_i is the relative volume abundance of N_2 and O_2 , $\left(\frac{d\sigma}{d\Omega} \right)_{\pi}^{RR,i} (J_i, T)$ is the differential backscatter cross-section for single lines of the pure

rotational Raman spectrum, and T_{atm} is the atmospheric roundtrip transmission, which can be separated into two contributions due to air molecules and aerosol particulates as:

$$T_{atm} = T_m \cdot T_a, \tag{2}$$

where the subscripts m and a refer to atmospheric molecules and aerosol particulates, respectively.

The atmospheric molecule roundtrip transmission can be expressed as:

$$T_m = e^{-2\int_0^z \alpha_m(z')dz'}, \tag{3}$$

where α_m is the atmospheric molecule extinction coefficient (m^{-1}). The atmospheric aerosol roundtrip transmission can be expressed as:

$$T_a = e^{-2AOD}, \tag{4}$$

where aerosol optical depth (AOD) is the integral of the aerosol extinction coefficient in the vertical direction.

The number of photons corresponding to the intensity of the solar background light received at wavelength λ can be evaluated as [14]:

$$N_B(\lambda) = ft\eta \frac{\lambda}{hc} P_B \pi \left(\frac{FOV}{2}\right)^2 \Delta\lambda A_R \frac{2\Delta z}{c}, \tag{5}$$

where P_B is the amount of sky spectral radiance ($Wm^{-2}sr^{-1}nm^{-1}$), FOV is the field of view of the receiving telescope, and $\Delta\lambda$ is the interference filter bandwidth (nm). Apart from Raman backscatter and sky background contributions, the final signal also consists of the detector dark counts, which can be expressed as:

$$N_D = ftC_D \frac{2\Delta z}{c}, \tag{6}$$

where C_D is the dark count rate (s^{-1}).

The signal-to-noise ratio (SNR) of two rotational Raman channels can be expressed as [15–17]:

$$SNR_i(z) = \frac{N_{RRi}}{\sqrt{N_{RRi}(z, T) + N_{Bi}(\lambda) + N_{Di}}}, (i = 1, 2), \tag{7}$$

where $i = 1, 2$ represents the two rotational Raman channels, respectively.

According to the error theory, the SNR of the two rotational Raman channels can be combined as [18]:

$$SNR(z) = \frac{1}{\sqrt{SNR_1^{-2} + SNR_2^{-2}}}. \tag{8}$$

The atmospheric temperature can be derived as [12]:

$$Q = \frac{N_{RR1}}{N_{RR2}} = \exp\left(\frac{a}{T} + b\right). \tag{9}$$

According to the error propagation formula, the statistical errors of Q and T can be expressed as [18]:

$$\Delta Q = Q \sqrt{\frac{N_{RR1} + N_{B1} + N_{D1}}{N_{RR1}^2} + \frac{N_{RR2} + N_{B2} + N_{D2}}{N_{RR2}^2}} \tag{10}$$

$$\Delta T = \frac{\partial T}{\partial Q} \Delta Q. \tag{11}$$

From Equations (8)–(11), the relationship between the statistical error of temperature and the system signal-to-noise ratio can be obtained as follows [19]:

$$\Delta T = \frac{\partial T}{\partial Q} Q \cdot \frac{1}{SNR'} \tag{12}$$

where:

$$\Theta = \frac{1}{Q} \cdot \frac{\partial Q}{\partial T'} \tag{13}$$

which can then characterize the temperature measurement sensitivity of the LiDAR system.

3. Numerical Analysis

The optical setup of the proposed Raman temperature LiDAR is shown in Figure 1. A Nd:YAG laser was used as the source. After it passed through the beam expander (BE), the angle of divergence of the Nd:YAG laser beam significantly decreased, resulting in a smaller field-of-view of the receiver that helped suppress solar background light. The backscattered signal generated by the expanded laser beam interacting with atmospheric components was received by a Cassegrain telescope, passed through an optical fiber, and then entered the polychromator, which was used to select specific wavelengths. Solar background radiation can seriously affect the detection-related performance of LiDAR systems. Ultranarrow interference filters (IF) inside the polychromator were used to suppress solar background radiation. Two photomultipliers (PMT) were placed after the IF to collect the selected radiation signals.

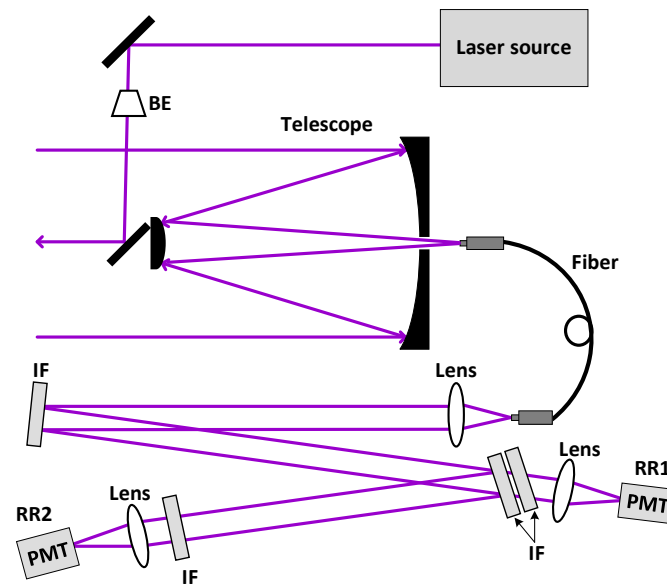


Figure 1. The optical setup of the proposed Raman temperature LiDAR.

The design goal is that under most weather conditions (aerosol optical depth greater than 0.5, aerosol roundtrip transmission less than 0.37) [20,21], the Raman temperature LiDAR maximum detection range should be greater than 4 km in daytime and greater than 10 km at night. To achieve the expected performance, the hardware parameters that met the target performance were selected through a simulation analysis.

Most Raman temperature LiDARs operate at wavelengths of 355 nm or 532 nm [22]. To compare the performance of Raman LiDARs in terms of measuring temperature at wavelengths of 355 nm or 532 nm, we assumed that the pulse energy of the laser was 200 mJ, the radius of the telescope was 0.2 m, and the receiving field of view was 0.75 mrad for the simulations. The parameters of the interference filters of the Raman LiDAR were selected from references [5,6]. The other parameters are shown in Table 1. The statistical errors in

the temperature measured by Raman LiDARs with wavelengths of 532 nm and 355 nm are shown in Figure 2. The temperature statistical error in the figure has been normalized. The Raman temperature measuring LiDAR operating at a wavelength of 532 nm has a larger detection range in night observation due to its higher optical efficiency and lesser atmospheric extinction. The Raman LiDAR operating at a wavelength of 355 nm has a larger backscattering cross-section and a smaller solar background, so that the temperature uncertainty is less during daytime detection. According to the selected detection target, the Raman LiDAR operating at a wavelength of 355 nm has a better detection performance in the daytime and at night, below 10 km. Therefore, 355 nm was chosen as the laser wavelength.

Table 1. Parameter values of the Raman LiDAR used in the simulation for laser wavelengths of 532 nm and 355 nm.

Metrics	Technical Performance Requirements
Laser pulse energy (mJ)	1–100
Laser repetition rate (Hz)	100
Receiver telescope radius (m)	0.01–0.5
Receiver field of view (mrad)	0.3–0.6
Integration time (s)	3600
Range resolution Δz (m)	15
Optical emission efficiency	0.8
Optical receiving efficiency	0.2
Detector quantum efficiency	0.3@355 nm, 0.4@532 nm
Dark count (s^{-1})	300
Interference filter central wavelength (nm) and bandwidth (nm)	IF1: 353.9–354.7, 0.1–0.3 IF2: 352–353.8, 0.1–0.7
Sky spectral radiance P_B ($Wm^{-2}sr^{-1}nm^{-1}$)	0.03@355 nm, 0.12@532 nm

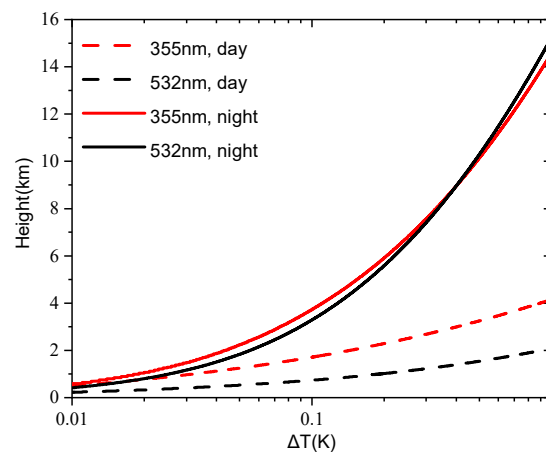


Figure 2. Temperature statistical error of 355 nm and 532 nm Raman LiDAR.

After the laser wavelength was selected as 355 nm, the center wavelength of the temperature channel interference filter was selected by analyzing the PRR spectrum. The temperature sensitivity of the pure rotational Raman spectrum of nitrogen was defined as [23]:

$$\kappa = \frac{\sigma_{N_2}(j, T_1) - \sigma_{N_2}(j, T_2)}{T_1 - T_2}, \tag{14}$$

where σ_{N_2} is the pure rotational Raman spectral intensity of nitrogen, j is the rotational quantum state, and T is the atmospheric temperature. The temperatures T_1 and T_2 were taken as 305 K and 300 K, respectively. The temperature sensitivity of the pure rotational Raman spectrum can be obtained by a derivation of the intensity of the pure rotational Raman spectrum from Equation (14). The sensitivity and intensity of the pure rotational Raman spectrum of nitrogen are shown in Figure 3. The temperature channel interference filter should be selected considering three factors: (1) Raman spectrum temperature sensitivity, (2) Raman spectrum intensity, and (3) The sufficient suppression of elastic signals. Figure 3 shows that when the temperature sensitivity of the Raman spectrum is negative, the temperature sensitivities of the rotational Raman spectra corresponding to $j = 4$ and $j = 6$ are greater. The temperature sensitivity of $j = 4$ is 4% higher than that of $j = 6$, and the Raman spectrum intensity is 23% lower. Because $j = 4$ and $j = 6$ are close to the emission wavelength of the laser (355 nm), there is a tradeoff between high Raman spectrum temperature sensitivity and intensity and the sufficient suppression of elastic signals. The central wavelength of IF1 should be between $\lambda(j = 4) = 354.35$ nm and $\lambda(j = 6) = 354.15$ nm, and close to 354.15 nm; it was set to 354.2 nm. When the temperature sensitivity of the Raman spectra is positive, the temperature sensitivity of the rotational Raman spectra corresponding to $j = 14$ and $j = 16$ is greater. The temperature sensitivity of $j = 14$ is 2% less than that of $j = 16$, and the Raman spectrum intensity is 36% greater. Therefore, the central wavelength of IF2 should be between $\lambda(j = 14) = 353.35$ nm and $\lambda(j = 16) = 353.15$ nm, and close to 353.35 nm; it was set to 353.3 nm.

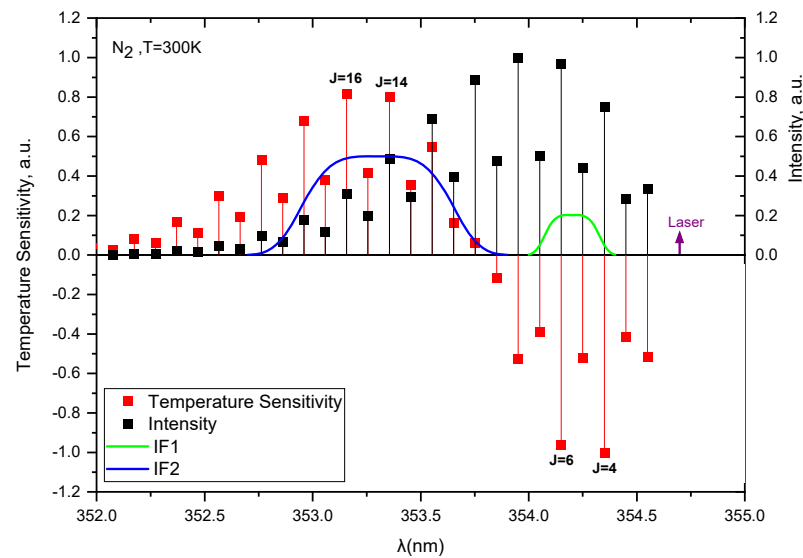


Figure 3. Pure rotational Raman spectrum of nitrogen and temperature sensitivity of Raman spectrum.

After the central wavelength of the interference filter and the bandwidth have been selected based on the minimum temperature statistical error, the PRR spectrum interval of nitrogen is about 0.1 nm when the laser wavelength is 355 nm. Therefore, to extract multiple rotational Raman spectra and increase the signal intensity, the bandwidth of the interference filter should be greater than 0.1 nm. The two interference filters should extract signals from the positive and negative temperature correlation parts of the rotational Raman spectrum, respectively. In addition, it is necessary to ensure that the transmission curves of the two interference filters do not coincide. Finally, it is necessary to consider the sufficient suppression of elastic signals by low-rotation quantum number channels. Therefore, the bandwidth variation ranges of interference filters IF1 ($\Delta\lambda_1$) and IF2 ($\Delta\lambda_2$) were selected as 0.1 nm–0.3 nm and 0.1 nm–0.7 nm, as shown in Figure 3. According to the parameters in Table 1, a contour map of the temperature statistical error and its variation with a bandwidth within this range was drawn, as shown in Figure 4a. This figure shows that the optimal value of $\Delta\lambda_1$ is 0.3 nm. However, when $\Delta\lambda_1$ is 0.2 nm, the temperature statistical error is only 11% higher than at 0.3 nm. Considering the full suppression of

elastic signals, and to leave more margin for later installation and adjustment, $\Delta\lambda_1$ was selected as 0.2 nm. After $\Delta\lambda_1$ was selected, it can be seen from Figure 4b that the optimal $\Delta\lambda_2$ was 0.5 nm. When $\Delta\lambda_2$ is greater than 0.5 nm, the temperature sensitivity and intensity of the multiple selected rotational Raman spectra are low, but an increase in $\Delta\lambda_2$ leads to an increase in the received solar background noise, which leads in turn to an increase in the statistical error of the temperature.

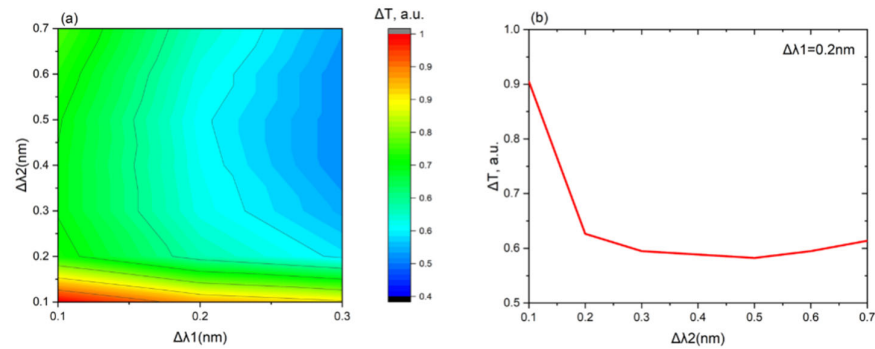


Figure 4. (a) Contour plot of temperature statistical error versus bandwidth; (b) $\Delta\lambda_1 = 0.2$ nm, temperature statistical error varies with $\Delta\lambda_2$.

As the laser pulse energy, telescope field of view, and telescope receiving aperture do not affect the temperature measurement sensitivity of the system (see Equation (13)), the above parameters can be optimized according to the SNR. The first step is to determine the signal-to-noise ratio that corresponds to the maximum detection distance. According to the precision requirements of WMO for temperature detection, the maximum detection distance is defined when the statistical error of the temperature is 1.5 K [24]. According to Equation (12), taking the tropospheric temperature range of the U.S. Standard atmosphere as about 200 K–300 K and the average value of $1/\Theta$ as 200 K–300 K, the SNR is about 80. z_{\max} can then be defined corresponding to $SNR(z_{\max}) = 80$ as the maximum detection distance.

Simulations were carried out to analyze the influence of the pulse energy at the selected laser wavelength of 355 nm and the optical parameters of the interference filter. According to the parameters in Table 1, different pulse energies were simulated under different aerosol roundtrip transmissions, and a detection distance curve was obtained, as shown in Figure 5a. From Figure 5a, it can be seen that under the same aerosol roundtrip transmission, the larger the laser pulse energy, the longer is the detection distance. In addition, when the aerosol roundtrip transmission was low (less than 0.1), there was little difference between the maximum detection distances of different laser pulse energies. When the aerosol roundtrip transmission was high, the detection range of the Raman LiDAR with a pulse energy of 30 mJ was 29% greater than that with 15 mJ. Figure 5b shows the detection distances at different pulse energies of the laser under the roundtrip transmission of an aerosol of 0.37 and the corresponding rate of increase in the detection distance. Figure 5b shows that the detection distance increased at larger scales of pulse energy of the laser, but the rate of increase was low. It also shows that the detection distance increased slowly once the pulse energy of the laser had exceeded 40 mJ. When the pulse energy was 30 mJ, the detection distance was 4.11 km. Given the design goal, whereby the maximum range of detection needed to be greater than 4 km during the daytime, we set the pulse energy to 30 mJ.

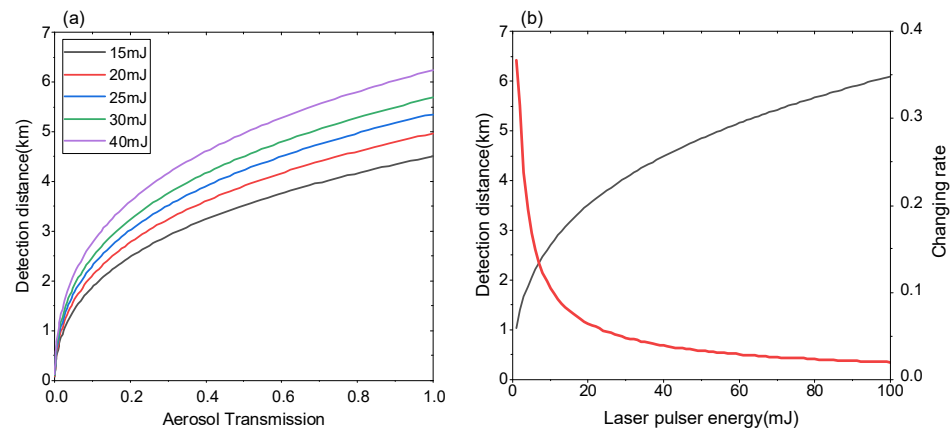


Figure 5. (a) Maximum detection range of Raman LiDAR as a function of aerosol roundtrip transmission as obtained from simulated SNR curves at four values of pulse energy: 15 mJ (black), 20 mJ (red), 25 mJ (blue), 30 mJ (green), and 40 mJ (purple) during daytime; (b) maximum detection distance as a function of the pulse energy of the laser (left axis, black) under roundtrip transmission of aerosol of 0.37, and the corresponding rate of increase in the detection distance (right axis, red).

After the laser wavelength of 355 nm, the optical parameters of the interference filter, and the laser pulse energy of 30 mJ were selected, according to other parameters in Table 1, the signals of different receiving fields of view under different aerosol roundtrip transmission conditions in the daytime were simulated, and a detection distance curve was obtained, as shown in Figure 6. From Figure 6, it is apparent that the smaller the receiving field of view, the longer is the detection distance. When the aerosol roundtrip transmission is low (less than 0.1), the maximum detection distance of different fields of view makes little difference. In the case of high aerosol roundtrip transmission, the maximum detection distance with a receiving field of view of 0.3 mrad is 28% greater than that of 0.6 mrad. In addition, beam divergence of the expanded laser beam in the Raman LiDAR system used in this study was 0.2 mrad. To achieve a better detection effect, the field of view of the telescope should be greater than 0.2 mrad. Therefore, the field of view of the telescope was selected as 0.3 mrad.

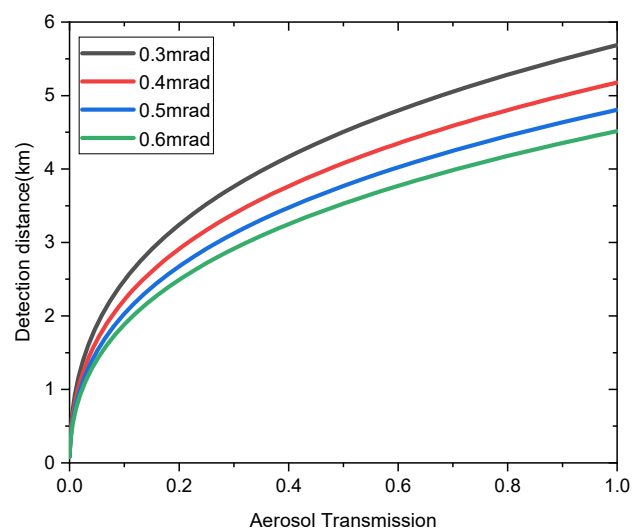


Figure 6. Maximum detection range of Raman LiDAR as a function of aerosol roundtrip transmission as obtained from simulated SNR curves at four values of telescope field of view: 0.3 mrad (black), 0.4 mrad (red), 0.5 mrad (blue), and 0.6 mrad (green), in daytime.

After a laser with a wavelength of 355 nm and a laser pulse energy of 30 mJ and a receiving field of view of 0.3 mrad were selected, the signals of receiving telescopes with

different telescope radii under different aerosol roundtrip transmission conditions were simulated according to the parameters in Table 1, and a detection distance curve was obtained, as shown in Figure 7. From Figure 7, it can be seen that under the condition of the same aerosol roundtrip transmission, the larger the radius of the receiving telescope, the longer will be the detection distance. When the aerosol roundtrip transmission is low (less than 0.1), the maximum detection distance of different telescope radii makes little difference. In the case of a high aerosol roundtrip transmission, the LiDAR detection range with a telescope radius of 0.15 m is only 6% greater than with a radius of 0.125 m. Figure 8 shows the detection distance of different receiving radii and the corresponding changes in detection distance with an aerosol roundtrip transmission of 0.37. It can be seen from Figure 8a that the detection distance increases at longer receiving radii, but the growth rate is slower, as shown in Figure 8b. This occurs because the receiving aperture is increased, which is conducive to receiving more echo signals, but also receives more background noise. Figure 8b shows that the detection distance increases very slowly after the receiving radius becomes greater than 0.2 m. Therefore, the receiving radius should not be greater than 0.2 m to obtain a higher cost-performance because the cost of the receiving telescope increases sharply with aperture. Based on comprehensive considerations, the radius of the receiving telescope was determined as 0.125 m.

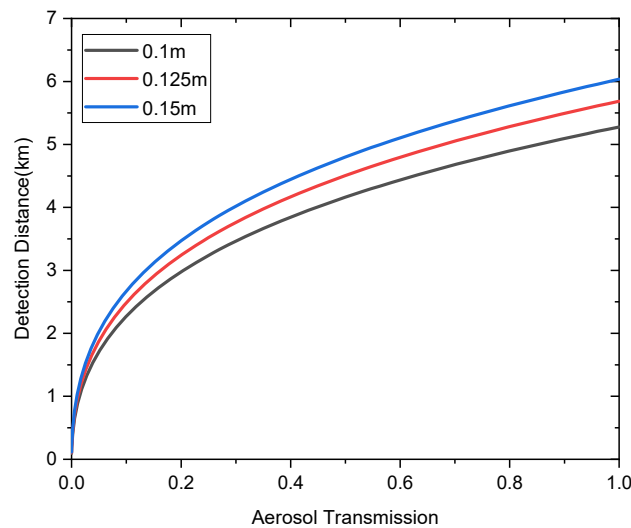


Figure 7. Maximum detection range of Raman LiDAR as a function of aerosol roundtrip transmission as obtained from simulated SNR curves at three values of telescope radius: 0.1 m (black), 0.125 m (red), and 0.15 m (blue) in daytime.

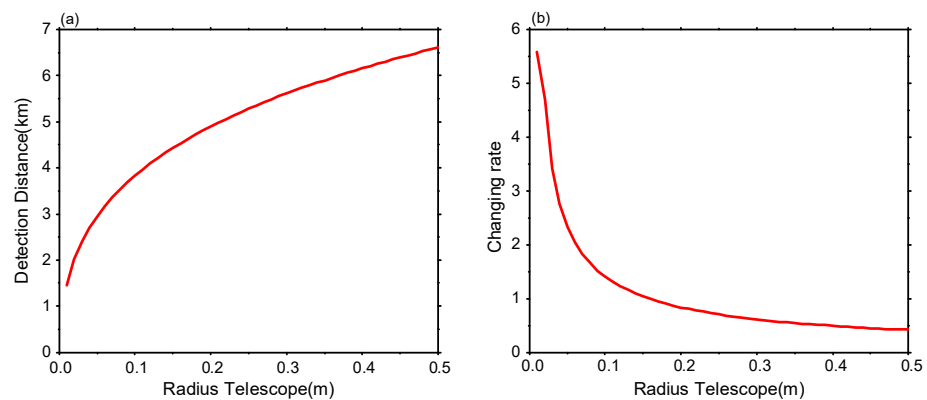


Figure 8. (a) Maximum detection distance as a function of telescope radius and (b) the corresponding rate of change in the detection distance under the condition of an aerosol roundtrip transmission of 0.37.

When the laser wavelength is 355 nm, the center wavelength and the bandwidth of the two interference filters are 354.2 nm and 0.2 nm, 353.3 nm and 0.5 nm, respectively, the laser pulse energy is 30 mJ, the receiving field of view is 0.3 mrad, and the telescope radius is 0.125 m. The final optimized parameters are shown in Table 2. According to other parameters in Table 1, the maximum detection range of the LiDAR system was simulated in the daytime and at night under different aerosol roundtrip transmissions, as shown in Figure 9. Figure 9 shows that when the roundtrip transmission of aerosol is less than 0.37, the detection distance is greater than 4 km in the daytime, while it was greater than 10 km at night. Using a laser with an energy of only 30 mJ with a receiving telescope with an aperture of 250 mm can theoretically yield a range of detection of 10 km.

Table 2. Optimal values of laser pulse energy, receiver telescope radius, receiver field of view, and interference filter central wavelength and bandwidth.

Metrics	Technical Performance Requirements
Laser pulse energy (mJ)	30
Receiver telescope radius (m)	0.125
Receiver field of view (mrad)	0.3
Interference filter central wavelength (nm) and bandwidth (nm)	IF1: 354.2, 0.2 IF2: 353.3, 0.5

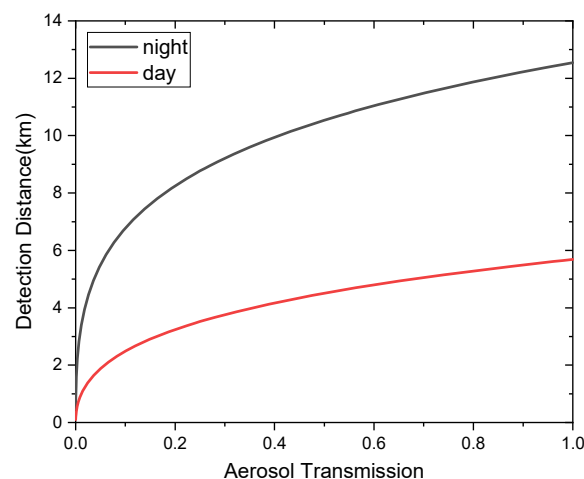


Figure 9. Raman LiDAR maximum detection distance as a function of aerosol roundtrip transmission for daytime (red) and nighttime (black).

4. Measurement Examples

In 2022, a Raman temperature LiDAR with the optimal parameters discussed in the previous section and listed in Table 2 was installed and commissioned in Guangzhou (113.920647° E, 22.498085° N), China. On 11–14 October 2022, the weather in Guangzhou was clear. Figure 10 shows the original echo signals received by two rotating Raman channels at night on 11–14 October 2022, at a resolution of 15 m and with an integration time of 60 min. According to Figure 3, the intensity of the rotational Raman spectrum received by channel RR2 was weaker than that received by channel RR1, because of which the intensity of the echo signals of the latter should have been weaker than that of the former. However, Figure 10 shows that the intensity of the echo signals of channel RR2 was slightly higher than that of channel RR1, mainly because the latter was close to the wavelength of emission of the laser. Two interference filters were superimposed in channel RR1 to completely suppress the elastic signals, but this reduced its optical efficiency. Figure 10 shows that the proposed Raman temperature system had a relatively good signal.

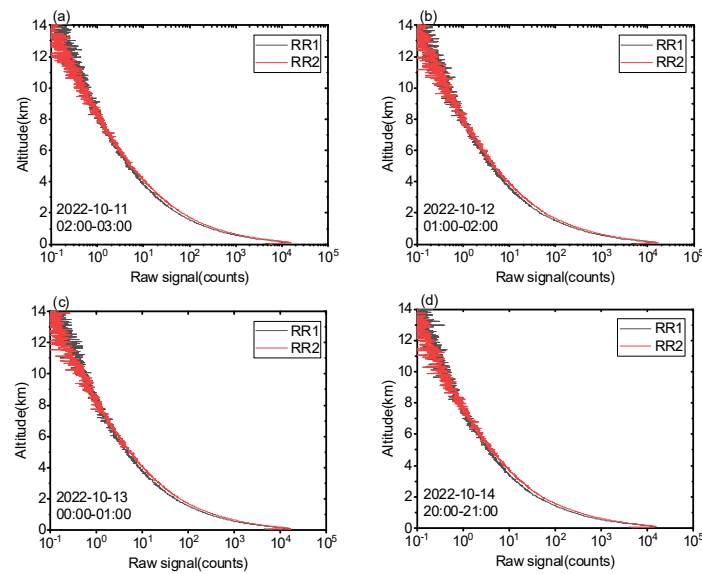


Figure 10. Raw data measured by the Raman temperature LiDAR. Measurements on 11, 12, 13, and 14 October 2022 (a–d).

The Raman temperature LiDAR obtained good observation results; the measurement results during the night are shown in Figure 11. In the process of retrieving the atmospheric temperature, the distance resolution of the original data obtained by the Raman system was 15 m. A moving average is performed on every 20 points below 3 km, every 30 points between 3 and 5 km, and every 100 points above 5 km. Figure 11a,c,e,g show that the LiDAR detection results are in good agreement with the radiosonde. Figure 11b,d,f,h show that the statistical error of the Raman temperature LiDAR measurement is less than 1.5 K below 8 km, and is smaller than 2 K below 8–10 km. The deviation between the measurements of the LiDAR and the radiosonde was approximately smaller than 4 K up to 4.5 km. A relatively larger absolute deviation was observed, mainly because the location from which the radiosonde was launched was far from that of the Raman LiDAR, about 150 km. The corresponding correlation between the Raman temperature LiDAR and the radiosonde is shown in Figure 12, from which it is clear that the results were highly consistent, with a minimum correlation of 0.83 and a maximum correlation of 0.94.

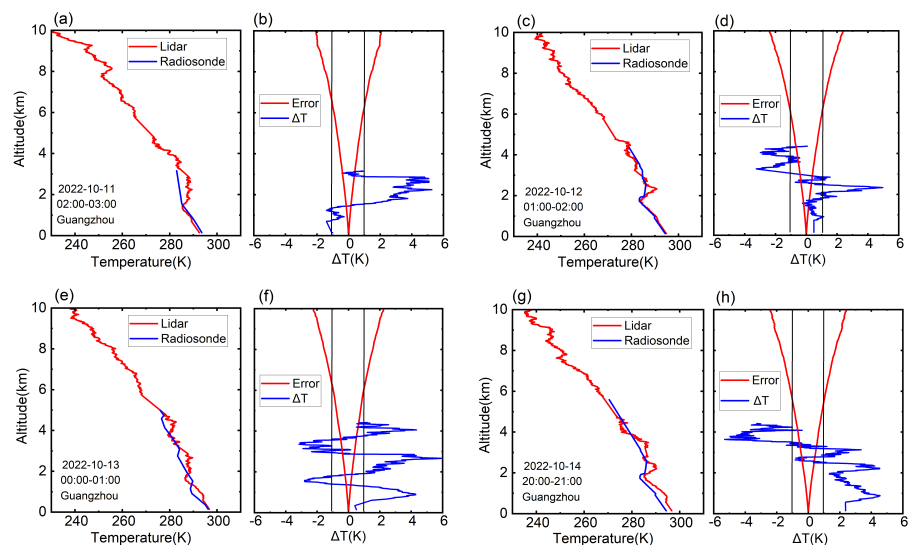


Figure 11. Temperature profiles measured by the Raman temperature LiDAR and the radiosonde on 11, 12, 13, and 14 October 2022 are shown in (a,c,e,g), respectively, and the corresponding statistical errors and deviations between the LiDAR and the radiosonde are shown in (b,d,f,h).

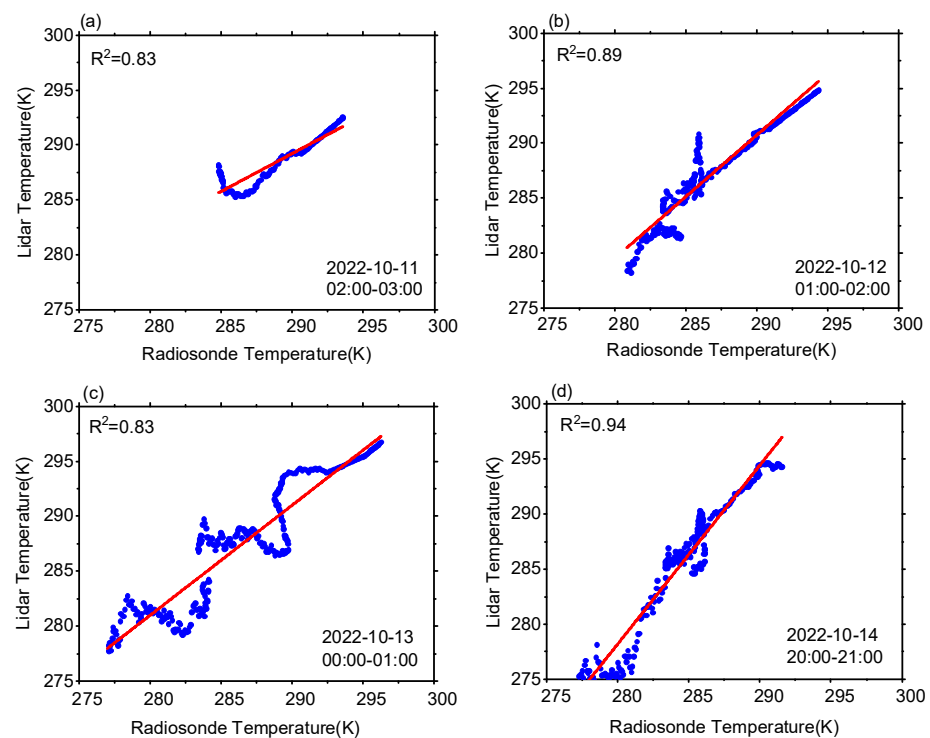


Figure 12. Correlation between the Raman temperature LiDAR and the radiosonde on 11–14 October 2022 (a–d).

Figure 13 shows the raw data and the temperature profiles observed during the daytime on 12 October 2022. Figure 13a shows that the Raman LiDAR had a relatively good signal at a distance of up to 5 km during the day. Figure 13b shows that the temperatures measured by the Raman temperature system and radiosonde were relatively consistent, and Figure 13c shows that the statistical error between them was smaller than 2 K below 5 km, while the deviation in temperature between the results of the LiDAR and the radiosonde did not exceed 4 K below 4.5 km. The correlation is shown in Figure 13d, with a correlation coefficient of up to 0.81. These results show that the Raman temperature LiDAR reached a maximum distance of detection of temperature of 5 km in the daytime and that of 10 km at night. This means that all the design objectives had been achieved. The proposed low-energy (30 mJ) Raman temperature system with a small aperture (250 mm) delivers competitive performance to a previously developed Raman temperature system that used a laser with a pulse energy of 800 mJ and a receiving telescope with an aperture of 900 mm.

Figure 14 shows the time height contour of atmospheric temperature on 11–14 October 2022. A 60 min moving average of the data is included. Temperature data over 5 km in the daytime were obtained by splicing atmospheric models [25]. The evolution trend of the boundary layer on that day can be seen from Figure 14, e.g., the near-surface temperature starts to rise at about 6 o'clock every day and starts to drop after 18 o'clock. This is the time between sunrise and sunset in October in Guangzhou. This proves from one aspect that the observed results of this Raman LiDAR are reliable. Figure 14 show that the developed Raman temperature LiDAR can work continuously all day under clear sky. This means that the LiDAR system developed in this study can provide continuous temperature data for the study of tropospheric atmospheric activities.

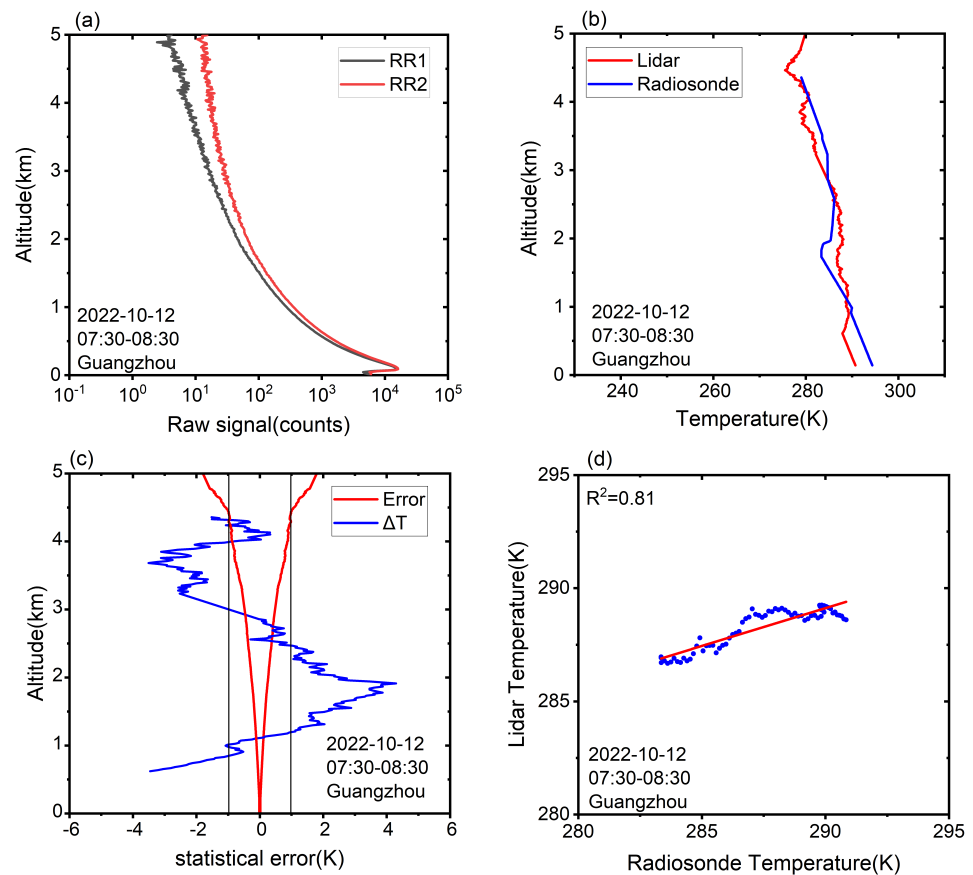


Figure 13. (a) Raw data measured by the Raman temperature LiDAR. (b) Temperature profiles (red) measured by the Raman temperature LiDAR and radiosonde (blue). (c) The corresponding temperature statistical error (red), and the deviation between the results of LiDAR and radiosonde (blue). (d) Correlation between the Raman temperature LiDAR and the radiosonde on 12 October 2022.

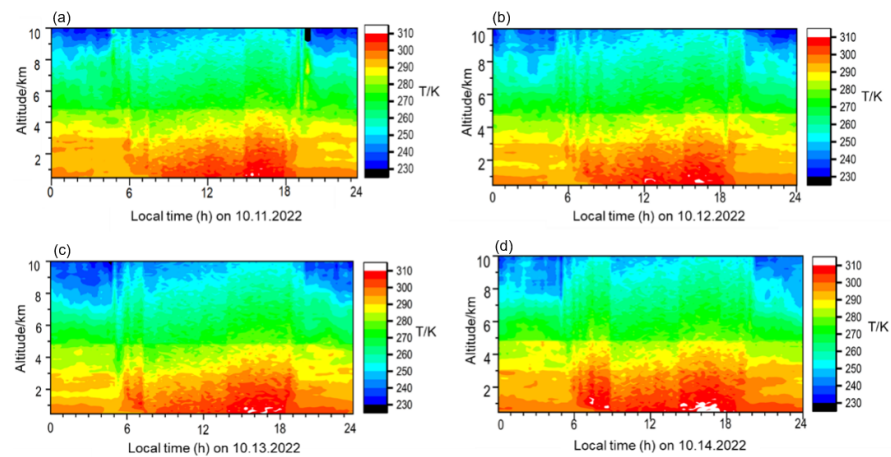


Figure 14. Time–height contour plot of all-day temperature measured by the LiDAR system developed in this study: (a) on 11 October 2022, (b) on 12 October 2022, (c) on 13 October 2022, and (d) on 14 October 2022.

5. Conclusions

In this paper, a simulation theory for a Raman temperature LiDAR system is proposed. Around the designed detection target, a series of echo signals under different aerosol transmission levels were simulated to study the influence of various hardware parameters on the design target. Through simulation and parameter optimization, a Raman temperature

LiDAR with a low energy and a small aperture was established. It satisfies the design requirements of being able to detect the daytime temperature at a distance longer than 5 km and the nighttime temperature at a distance greater than 10 km under most weather conditions (roundtrip transmission of aerosol of less than 0.37). In a field test in Guangzhou, the Raman temperature LiDAR developed in this study successfully observed continuous temperature in the troposphere. The retrieved atmospheric temperature profile was in good agreement with the results of radiosonde. The maximum correlation between the Raman temperature LiDAR and the radiosonde was 0.94 at night and 0.81 during the day. These results show that the proposed Raman temperature LiDAR with low energy and a small aperture can provide reliable temperature data in the troposphere throughout the day. These data can be applied to the study of atmospheric dynamics and climate change, which is of great significance in further understanding atmospheric activities in the troposphere.

Author Contributions: Conceptualization, J.X.; methodology, B.X.; software, B.X.; validation, H.Y.; formal analysis, H.Y.; investigation, W.X.; resources, H.Y.; data curation, C.C.; writing original draft preparation, B.X.; writing—review and editing, J.X.; visualization, Y.G.; supervision, J.X. and X.W.; project administration, D.S.; funding acquisition, Y.H. All authors have read and agreed to the published version of the manuscript.

Funding: National Natural Science Foundation of China (No. 42104146).

Institutional Review Board Statement: Not applicable.

Informed Consent Statement: Not applicable.

Data Availability Statement: Data underlying the results presented in this paper are not publicly available at this time, but may be obtained from the authors upon reasonable request.

Acknowledgments: Parts of this work were supported by Darsunlaser Technology Co., Ltd.

Conflicts of Interest: The authors declare no conflict of interest.

References

1. Su, J.; McCormick, M.P.; Lei, L. New Technique to Retrieve Tropospheric Temperature Using Vibrational and Rotational Raman Backscattering. *Earth Space Sci.* **2020**, *7*, e2019EA000817. [[CrossRef](#)]
2. Newsom, R.K.; Turner, D.D.; Goldsmith, J.E.M. Long-Term Evaluation of Temperature Profiles Measured by an Operational Raman Lidar. *J. Atmos. Ocean. Technol.* **2013**, *30*, 1616–1634. [[CrossRef](#)]
3. Radlach, M. *A Scanning Eye-Safe Rotational Raman Lidar in the Ultraviolet for Measurements of Tropospheric Temperature Fields*; University of Hohenheim: Stuttgart, Germany, 2009.
4. Dolgii, S.I.; Nevzorov, A.A.; Nevzorov, A.V.; Romanovskii, O.A.; Kharchenko, O.V. Intercomparison of Ozone Vertical Profile Measurements by Differential Absorption Lidar and IASI/MetOp Satellite in the Upper Troposphere–Lower Stratosphere. *Remote Sens.* **2017**, *9*, 447. [[CrossRef](#)]
5. Behrendt, A.; Nakamura, T.; Onishi, M.; Baumgart, R.; Tsuda, T. Combined Raman lidar for the measurement of atmospheric temperature, water vapor, particle extinction coefficient, and particle backscatter coefficient. *Appl. Opt.* **2002**, *41*, 7657–7666. [[CrossRef](#)]
6. Hammann, E.; Behrendt, A.; Le Mounier, F.; Wulfmeyer, V. Temperature profiling of the atmospheric boundary layer with rotational Raman lidar during the HD(CP)(2) Observational Prototype Experiment. *Atmos. Chem. Phys.* **2015**, *15*, 2867–2881. [[CrossRef](#)]
7. Wang, Y.; Tang, L.; Zhang, J.; Gao, T.; Wang, Q.; Song, Y.; Hua, D. Investigation of Precipitable Water Vapor Obtained by Raman Lidar and Comprehensive Analyses with Meteorological Parameters in Xi'an. *Remote Sens.* **2018**, *10*, 967. [[CrossRef](#)]
8. Cooney, J. Measurement of atmospheric temperature profiles by Raman backscatter. *J. Appl. Meteorol. Climatol.* **1972**, *11*, 108–112. [[CrossRef](#)]
9. Cooney, J.; Pina, M. Laser radar measurements of atmospheric temperature profiles by use of Raman rotational backscatter. *Appl. Opt.* **1976**, *15*, 602–603. [[CrossRef](#)]
10. Behrendt, A.; Reichardt, J. Atmospheric temperature profiling in the presence of clouds with a pure rotational Raman lidar by use of an interference-filter-based polychromator. *Appl. Opt.* **2000**, *39*, 1372–1378. [[CrossRef](#)]
11. Di Girolamo, P.; Marchese, R.; Whiteman, D.N.; Demoz, B.B. Rotational Raman Lidar measurements of atmospheric temperature in the UV. *Geophys. Res. Lett.* **2004**, *31*, L01106. [[CrossRef](#)]
12. Weng, M.; Yi, F.; Liu, F.; Zhang, Y.; Pan, X. Single-line-extracted pure rotational Raman lidar to measure atmospheric temperature and aerosol profiles. *Opt. Express* **2018**, *26*, 27555–27571. [[CrossRef](#)]

13. Weitkamp, C. *Lidar: Range-Resolved Optical Remote Sensing of the Atmosphere*; Springer Science & Business: Berlin/Heidelberg, Germany, 2006; Volume 102.
14. Nakajima, T.Y.; Imai, T.; Uchino, O.; Nagai, T. Influence of daylight and noise current on cloud and aerosol observations by spaceborne elastic scattering lidar. *Appl. Opt.* **1999**, *38*, 5218–5228. [[CrossRef](#)]
15. Spinhirne, J.D. Micro pulse lidar. *IEEE Trans. Geosci. Remote Sens.* **1993**, *31*, 48–55. [[CrossRef](#)]
16. Xian, J.; Sun, D.; Amoruso, S.; Xu, W.; Wang, X. Parameter optimization of a visibility LiDAR for sea-fog early warnings. *Opt. Express* **2020**, *28*, 23829–23845. [[CrossRef](#)]
17. Xu, W.; Yang, H.; Sun, D.; Qi, X.; Xian, J. Lidar system with a fast scanning speed for sea fog detection. *Opt. Express* **2022**, *30*, 27462–27471. [[CrossRef](#)]
18. Bevington, P.; Robinson, D.K. *Data Reduction and Error Analysis for Physical Sciences*; McGraw-Hill: New York, NY, USA, 2003.
19. Hua, D.X.; Uchida, M.; Kobayashi, T. Ultraviolet Rayleigh-Mie lidar for daytime-temperature profiling of the troposphere. *Appl. Opt.* **2005**, *44*, 1315–1322. [[CrossRef](#)]
20. Torres, O.; Bhartia, P.; Herman, J.; Sinyuk, A.; Ginoux, P.; Holben, B. A long-term record of aerosol optical depth from TOMS observations and comparison to AERONET measurements. *J. Atmos. Sci.* **2002**, *59*, 398–413. [[CrossRef](#)]
21. Colarco, P.; da Silva, A.; Chin, M.; Diehl, T. Online simulations of global aerosol distributions in the NASA GEOS-4 model and comparisons to satellite and ground-based aerosol optical depth. *J. Geophys. Res. Atmos.* **2010**, *115*, D14207. [[CrossRef](#)]
22. Summa, D.; Vivone, G.; Franco, N.; D'Amico, G.; De Rosa, B.; Di Girolamo, P. Atmospheric Boundary Layer Height: Inter-Comparison of Different Estimation Approaches Using the Raman Lidar as Benchmark. *Remote Sens.* **2023**, *15*, 1381. [[CrossRef](#)]
23. Sun, D.; Kobayashi, T. Basic Design of UV Rotational Raman Lidar for Temperature Measurement of the Troposphere. *Fukuoka Univ. Fac. Eng.* **1999**, *47*, 123–130.
24. Gustafsson, N.; Capaldo, M.; Estrada, B.O.; Quiby, J. Position Paper—Requirements of Observations for Regional NWP. AEG/NWP: Darmstadt, Germany, 2001.
25. Bo, L.; Hongxia, W.; Liang, Z.; Yufeng, W.; Dengxin, H. Data Splicing Method for LiDAR Detection Temperature Under Fog-Haze Condition. *Acta Opt. Sin.* **2020**, *40*, 0928003.

Disclaimer/Publisher's Note: The statements, opinions and data contained in all publications are solely those of the individual author(s) and contributor(s) and not of MDPI and/or the editor(s). MDPI and/or the editor(s) disclaim responsibility for any injury to people or property resulting from any ideas, methods, instructions or products referred to in the content.